Next-Generation Ultrasound Tunneling in Suspended Core Optical Fibers

Ricardo E. da Silva[1, 2] and David J. Webb[2]
[1]Institute of Physics Gleb Wataghin, University of Campinas (UNICAMP), Campinas, 13083-859, Brazil
[2]Aston Institute of Photonic Technologies (AIPT), Aston University, Birmingham, B4 7ET, UK
resilva@unicamp.br

ABSTRACT We demonstrate the spatial-temporal tunneling of high-frequency ultrasound inside a suspended core fiber (SCF) for the first time. An SCF composed of a 5 μm core suspended by nano bridges and four air holes is analytically and numerically investigated using the 2D and 3D finite element method. We reveal the propagation of ultrasonic modes in the SCF and describe the variation of their properties with increasing frequency from 1 to 100 MHz. Ultrasonic Gaussian-modulated pulses traveling with distinct frequencies (25 and 72 MHz) and bandwidths (56 and 10 MHz) are evaluated along the SCF length and time. The induced strain, pressure, and sensing responsivity are reviewed and discussed. Analytical and numerical results show highly confined effective single-mode propagation in the SCF core, amplifying strains along the fiber (up to 18 times) and pressures at the fiber output (up to 3 times). Compared to previous studies, the demonstrated SCF provides the widest 86 MHz high-responsivity bandwidth (with a -218 dB average and -75 dB maximum responsivity at 93 MHz). These achievements are promising for developing smaller, faster, and more efficient acousto-optic modulators for fiber lasers, enhancing simultaneous light-sound guidance and spatial resolution of fiber-based optoacoustic imaging sensors and neurostimulators in biomedicine.

Keywords: suspended core fibers, ultrasound propagation and tunneling, high-frequency ultrasonic devices, optoacoustic fiber sensors and neurostimulators.

1. INTRODUCTION

Optical fibers provide notable features enabling the development of cutting-edge ultrasonic devices for diagnosis and treatment of human organs, tissues, vessels, and arteries [1], [2], [3]. An electromagnetically immune, flexible, microscale and minimally invasive fiber can guide a pulsed laser to the biological tissue and measure its thermo-induced ultrasound signals [2]. The ultrasonic waves induce pressures and strains in the fiber changing the phase of guided optical modes [3], [4], [5]. Thus, optoacoustic fiber sensors employing standard single-mode fibers (SMFs) and fiber Bragg gratings (FBGs) offer significant sensitivities and compact sensor lengths (4 mm) compared to traditional piezoelectric transducers (PZT) [3]. However, whilst SMFs can measure ultrasound with high magnitudes at specific narrowband resonances around 25 and 70 MHz, they exhibit high attenuation from 40 to 60 MHz [4], [5], [6], [7]. In these resonances, the induced strains are mostly radially distributed in the fiber cladding, weakly overlapping with optical modes in the fiber core [8], [9]. This frequency (f)-induced attenuation limits the spatial resolution ($R \sim 1/f$) to detect microscale details (e.g., f = 25 - 125 MHz might measure tissue dimensions from 50 to 10 μm [1]).

Optical fibers are equally promising for ultrasonic neurostimulation to treat diseases such as depression, Alzheimer's, and dementia [1], [3], [10], [11], [12]. In this case, the pulsed laser excites an optical absorber deposited at the fiber tip [11], [12]. The absorber thermo-optic expansion generates ultrasonic waves which are focused on a brain region to stimulate a single or a group of neurons. This technique enables the stimulation of tissues with spatial resolutions as small as 39.6 μm [11]. Furthermore, high-frequency ultrasound enables the long-distance propagation of confined plane waves to reach the target [10], [11]. However, optoacoustic sensors and neurostimulators face critical constraints caused by the excessive attenuation in the fiber, absorber, and human tissues (0.6 – 1 dB $cm^{-1} MHz^{-1}$ [1], [10]). The neurostimulators (ultrasonic fiber emitters) require high pressures to reach the targets. Previous studies have reported high-pressure peaks (0.48 - 2.7 MPa) only at low-frequency resonances (centered around 8 - 13.9 MHz) with relatively broad bandwidths (8 - 50 MHz) [10], [11].

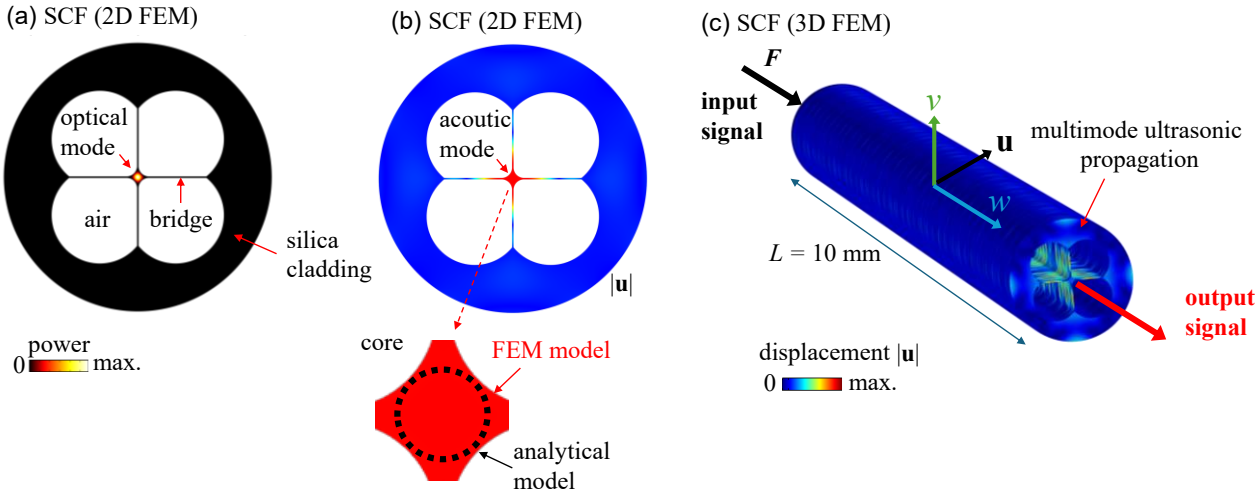

FIGURE 1. 2D SCF simulation of arbitrary (a) optical and (b) acoustic modes confined in the suspended core fiber (SCF) (inset indicates the core numerical and analytical models). (c) 3D SCF illustrates the ultrasonic input signal F exciting multiple ultrasonic modes. The multimode interference induces displacements along the length L ((green and blue arrows illustrate radial v and axial w components of the displacement vector u). The simulations are computed with the finite element method (FEM).

We have previously demonstrated that antiresonant hollow-core fibers (HCFs) offer notably higher ultrasound magnitudes compared to SMFs up to 100 MHz [13], [14]. In addition, we showed that suspended core fibers (SCF) are promising to confine standing ultrasonic waves at a narrowband resonance around 52.8 MHz [9]. Here, we demonstrate the space-time evolution of ultrasound in an SCF from 1 to 100 MHz using the 2D and 3D finite element method (FEM). The basic theoretical background to characterize the ultrasonic modes in the SCF is presented in Section 2, where the dispersive variation of the modal properties with frequency is numerically and analytically discussed. The propagation of Gaussian-modulated pulses with distinct center frequencies and bandwidths is studied in Section 3, indicating the frequency impact on induced displacements, strains, and pressures along the fiber length and with propagation time. The ultrasonic parameters and sensing responsivities are evaluated in Section 4, showing that SCFs can potentially guide, confine, and amplify ultrasonic waves in the fiber core, enabling exceptional features to advance the next generation of all-fiber ultrasonic devices (Section 5).

2. DISPERSION OF ULTRASONIC MODES IN THE SCF

Fig. 1(a) shows the simulated power distribution of the fundamental optical mode in the core of the modeled SCF using the 2D FEM (SCF dimensions and modeling methods are described in Appendix A). The optical mode is highly confined in the SCF core center, with evanescent power gradually decreasing to the edges formed by the air holes. Higher-order optical modes might be guided in the same core region, due to the high contrast between the silica and air refractive indices [8], [15].

Ultrasonic modes follow however a distinct propagation mechanism in optical fibers. Fig. 1(b) shows a 2D FEM simulated acoustic higher-order mode indicating its null (blue) and maximum (red) displacement modulus $|\mathbf{u}|$ at 100 MHz. The mode is distributed over the whole SCF cross-section, achieving a maximum displacement in the core. This modal confinement is defined by the SCF geometry, material and dimensions, and frequency of the input ultrasonic signal (air has a negligible effect on the ultrasonic modes in the silica). Fig. 1(c) shows the 3D FEM simulated $|\mathbf{u}|$ along a fiber length of L = 10 mm at 100 MHz (green and blue arrows illustrate radial v and axial w components of the displacement vector $\mathbf{u}$). The SCF's displacement pattern is indicative of the interference of multiple ultrasonic modes propagating along the fiber besides the mode shown in Fig. 1(b).

We evaluated the ultrasonic modes supported by the SCF from f = 1 to 100 MHz by using the 2D FEM as described in Appendix A. The modal properties are also analytically simulated in the SCF core, considering the 5 µm diameter inscribed circle illustrated in Fig. 1(b) (modeling is described in Appendix A). Fig. 2(a) shows the modes' displacement $|\mathbf{u}|$ distribution in the SCF over the frequency range. Fig. 2(b) shows the dispersion of the modes' group velocity c_g as a function of frequency f (c_g is compared to the silica's extensional, transversal, and Rayleigh velocities, c_E, c_T, and c_R, in which the velocities are normalized to c_E = 5740 m/s [7], [16], as described in Appendix A). The FEM simulated velocities are compared to the analytical group velocity of the ideal fundamental mode $LC(01)$ in the SCF core (dashed black line).

Fig. 2(b) shows that the FEM fundamental mode $L(01)$ propagates with nearly constant velocity approaching c_E at frequencies up to f = 10 MHz, inducing uniformly the displacements in the SCF in Fig. 2(a)). $L(01)$ tends to concentrate over the SCF cladding

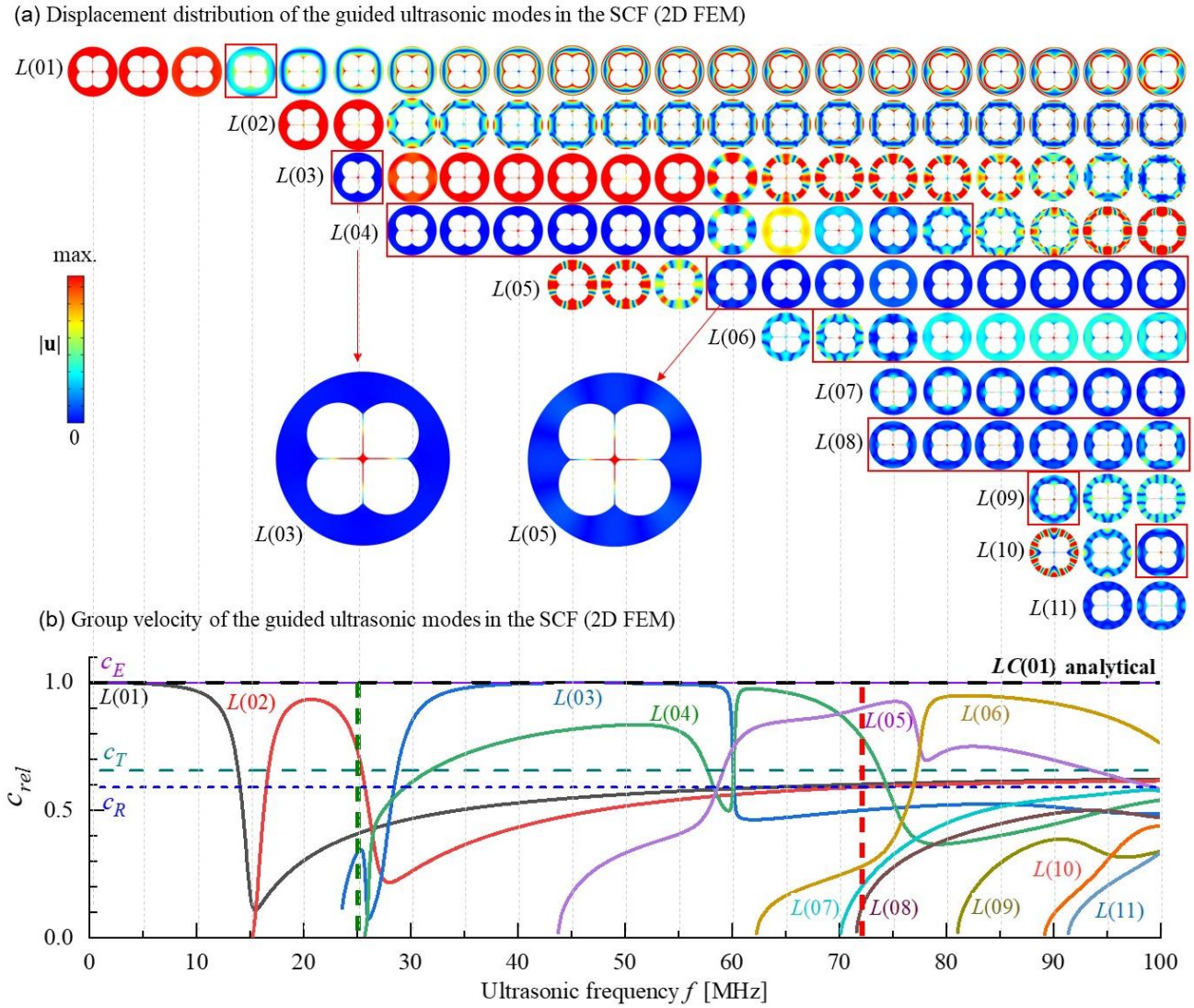

FIGURE 2. 2D FEM simulation of the (a) displacement distribution |u| and (b) relative group velocity c_{rel} of ultrasonic modes in the SCF from $f = 1$ to 100 MHz. The modes' group velocity c_g, silica's transversal c_T, and Rayleigh c_R velocity are normalized to the extensional velocity c_E. These velocities are compared to the analytical group velocity of an ideally single-mode circular SCF core (black dashed line).

and surface with c_g approaching c_T and c_R with increasing frequency. Similarly, other modes with low velocities induce mainly radially distributed displacements, showing maxima and nulls over the fiber cross-section. From $f = 30$ MHz, the higher-order modes $L(03)$, $L(04)$, $L(05)$, and $L(06)$ propagate with increasing velocities approaching c_E, showing highly confined displacements in the SCF core (insets in Fig. 2(a)). Modes approaching the analytical $LC(01)$ induce mostly axial displacements w in the SCF, contributing to effective single-mode propagation in the core. This is also indicated by modal wavenumber k and period Λ in Fig. 3(a) and 3(b). We note that the numerical and analytical curves highly overlap (~ 99 %) in the single-mode ranges, indicating strong interference of the first 6 modes (the remaining modes $L(07)$ - $L(11)$ contribute to displacements in the SCF cladding). The multimode interference is simulated in the SCF from $f = 1$ to 100 MHz (3D FEM modeling is described in Appendix A). The axial displacements $|w|$ are characterized along the SCF at the core center (radial components v are practically null due to axial symmetry so that $|\mathbf{u}| \sim |w|$). The wavelength Λ is measured with the fast Fourier transform (FFT) and amplitude peak-to-peak (APP) methods (Appendix A). Fig. 3(c) shows the 2D FFT spectrum normalized to the maximum $|w|$ (yellow) and compared to APP (white line) and the period of the first 6 modes (Fig. 3(b)). Differences between numerical and analytical results from $f = 15$ to 40 MHz (inset) might be caused by modes propagating with low velocities radially polarized in the SCF, showing dispersion curves deviating from the ideal mode $LC(01)$.

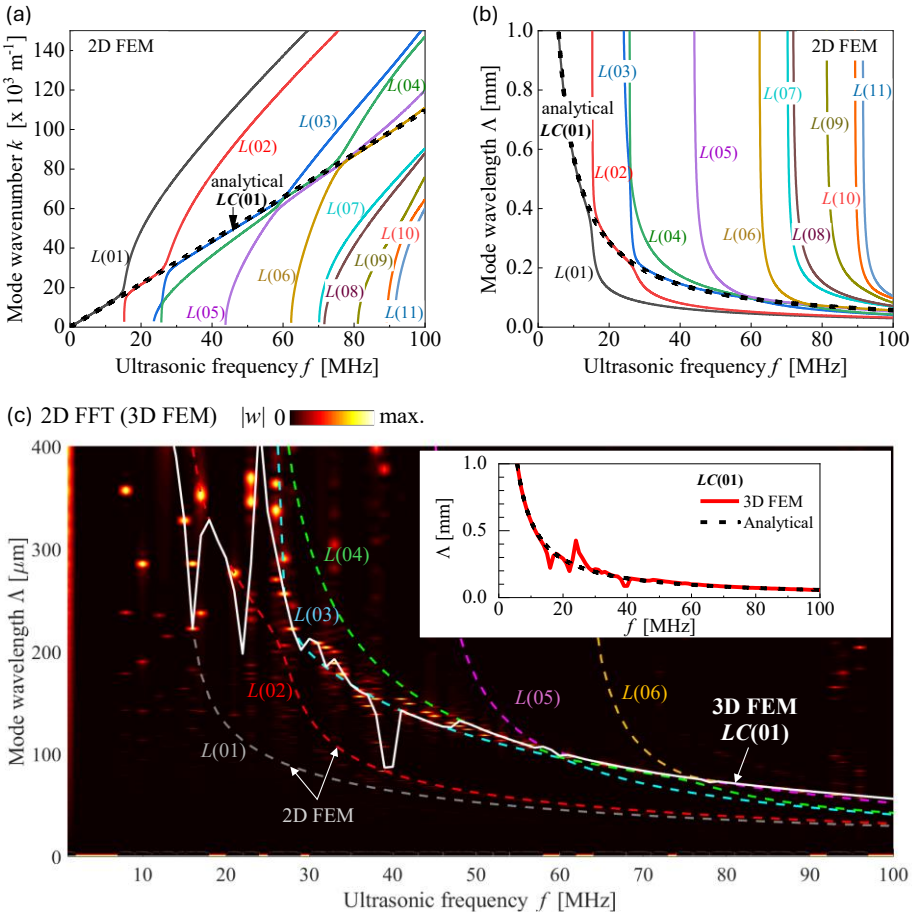

FIGURE 3. 2D FEM simulation of the SCF's ultrasonic modes' (a) wavenumber k and (b) wavelength Λ from f = 1 to 100 MHz. (c) 2D fast Fourier transform (FFT) of the 3D FEM simulated axial displacements $|w|$ in the SCF core center, indicating the multimode interference period Λ (yellow – max., black-null). Λ is also calculated with the amplitude peak-to-peak method (APP- white line) and compared to those of the first 6 modes in (b). The inset shows numerical and analytical results indicating a predominant single-mode $LC(01)$ in the SCF core.

3. ULTRASOUND TUNNELING IN THE SCF

3.1. Frequency-induced distortion of propagating gaussian-modulated pulses

We simulated the propagation of three ultrasonic Gausian-modulated pulses in the SCF, with center frequencies and bandwidths covering ranges of high frequency-induced dispersion and attenuation experienced in practical devices based on SMFs [3], [5]. This allows us to evaluate how effective single-mode guidance in the SCF core might contribute to minimizing dispersion effects. Fig. 4(a)-(c) show the temporal and spectral (FFT) profiles of the input pulses indicating the center frequency f (25 and 72 MHz), total time duration B_t (0.11 and 0.6 μs), and spectral bandwidth B_f (56 and 10 MHz) (3D FEM modeling is described in Appendix A). The pulses are applied at the SCF end, exciting the modes at frequencies defined in the pulse bandwidth (pulses' center frequencies are indicated with vertical lines in Fig. 2(b)). The 2D SCF views show the pulses propagating along the fiber length from t = 0.1 to 2 μs (insets show the 3D SCF at t = 2 μs). We note in Fig. 4(a) that the pulse propagates mostly distributed over the SCF cross-section, showing decreasing peak and low-amplitude trailing pulses along the length and time. In contrast, the pulse at f = 72 MHz having the same bandwidth (56 MHz) causes reduced trailing pulses, propagating mostly over the bridges and core. Similar ultrasound confinement in the SCF is observed for the narrow 10 MHz pulse in Fig. 4(c).

Fig. 5(a)-(c) show the pulses' displacements w at the SCF core ends during t = 2.7 μs (w is averaged over the core cross-section). Fig. 5(a) shows the pulse propagation inducing trailing pulses with the peak decreasing by 58 % at t = 2 μs. This distortion might be caused by modes propagating with distinct velocities and arriving at different times along the SCF (fast modes will arrive earlier at the fiber output) [17]. In addition, the modes' velocity abruptly changes in the frequency range, contributing to trailing pulses. Thus, modes radially distributed at f = 25 MHz appear to concentrate mostly in the SCF cladding, reducing displacements in the core.

The pulses at $f = 72$ MHz are strongly confined in the SCF bridges and core, showing respectively 3.4 and 2.5 times higher magnitudes at the SCF output, as shown in Fig. 5(b) and 5(c). Reduced trailing pulses are achieved for the narrow pulse (10 MHz), enhancing single-mode propagation in the SCF core, while decreasing the multimode dispersion effects along the fiber. Overall, the three pulses take about the same time to arrive at the SCF output ($t = 1.75$ µs), with a faster peak to the pulse in Fig. 5(b). The pulses' propagation times are consistent with the analytical extensional silica velocity estimated in Fig. 2(b).

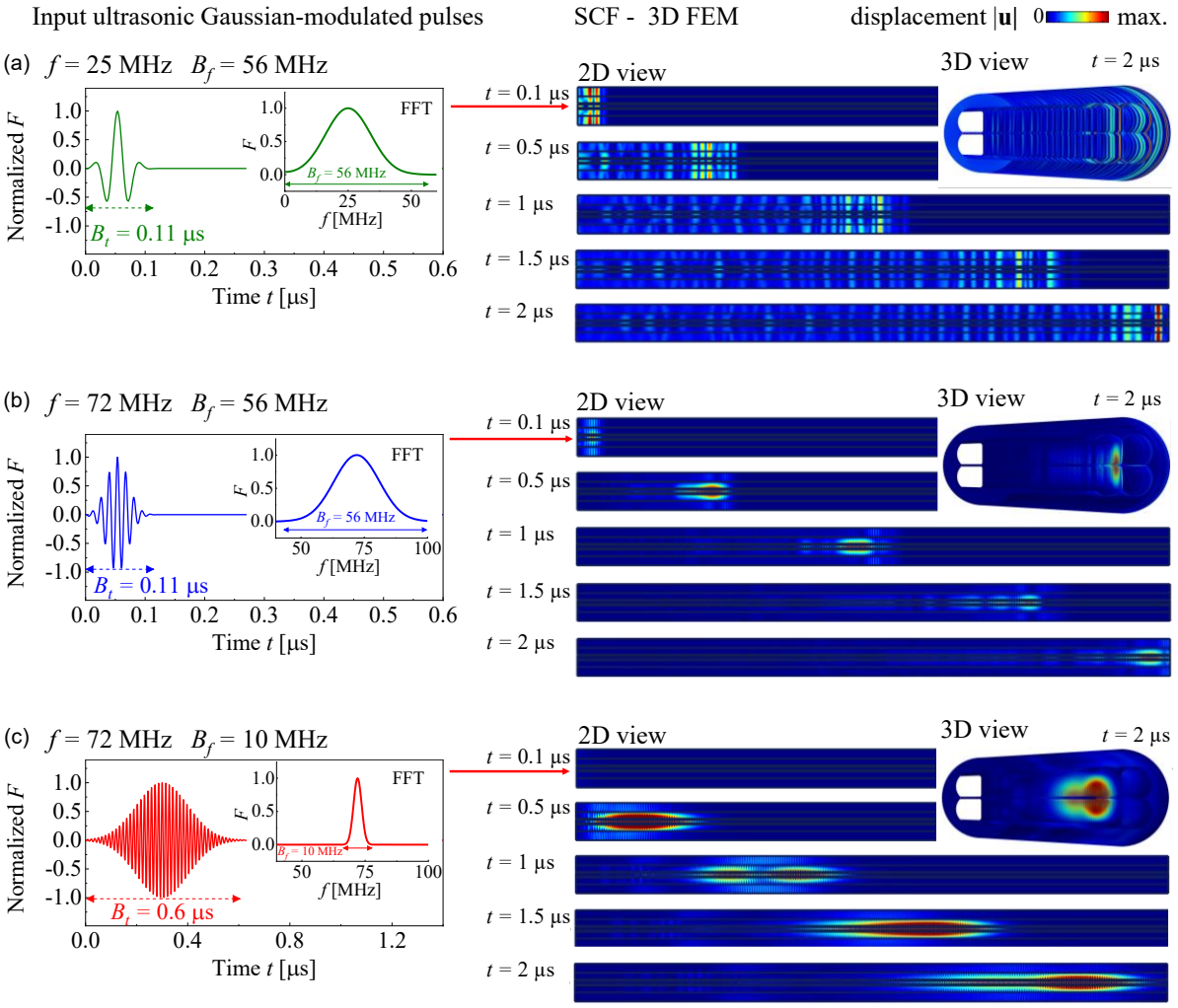

FIGURE 4. 3D FEM simulated ultrasonic Gaussian-modulated pulses propagating in the SCF at (a) $f = 25$ MHz ($B_f = 56$ MHz), (b) $f = 72$ MHz ($B_f = 56$ MHz) and (c) $f = 72$ MHz ($B_f = 10$ MHz) (2D views show the pulses from $t = 0.1$ to 2 µs with a 3D detail at $t = 2$ µs). The input pulses' temporal and spectral (FFT) profiles indicate the normalized magnitude F, total time duration B_t, and frequency bandwidth B_f.

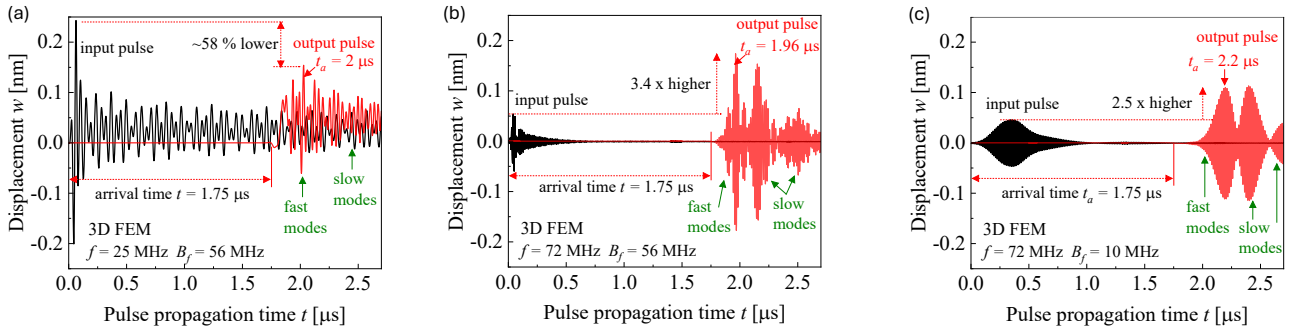

FIGURE 5. 3D FEM simulated ultrasonic Gaussian-modulated pulses in the SCF core input (black) and output (red) at (a) $f = 25$ MHz ($B_f = 56$ MHz), (b) $f = 72$ MHz ($B_f = 56$ MHz) and (c) $f = 72$ MHz ($B_f = 10$ MHz) during propagation up to $t = 2.7$ µs (axially induced displacement w is averaged over the core cross-section).

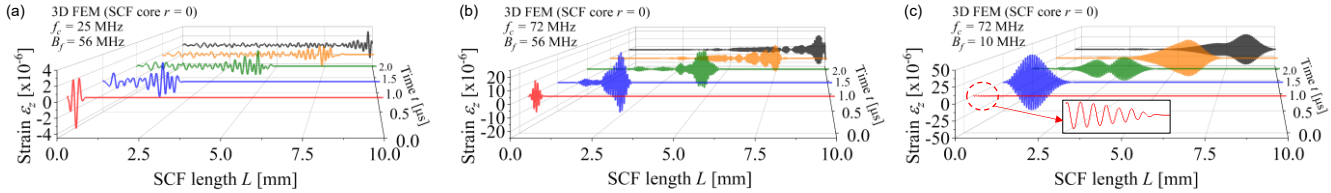

FIGURE 6. 3D FEM simulated axial strains ε_z induced by the ultrasonic pulses along the SCF core center at (a) f = 25 MHz (B_f = 56 MHz), (b) f = 72 MHz (B_f = 56 MHz), and (c) f = 72 MHz (B_f = 10 MHz) from t = 0.1 to 2 μs (5 steps). The inset shows a pulse's detail at t = 0.1 μs.

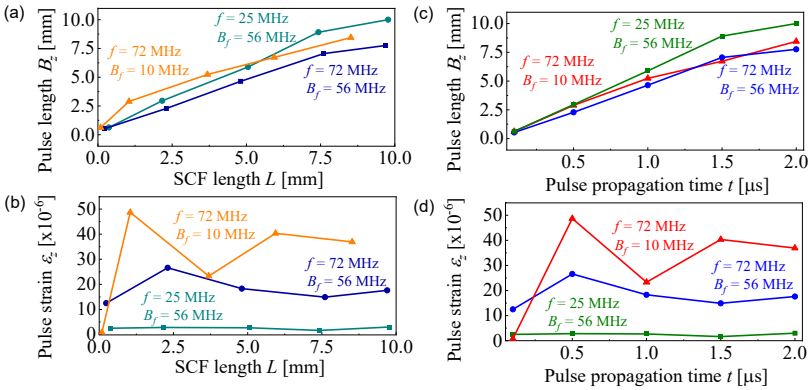

FIGURE 7. 3D FEM simulated pulses' length B_z and axial strain peak ε_z along the (a)(b) SCF length L and (c)(d) propagation time from t = 0.1 to 2 μs (5 steps).

3.2. Pulse induced strain and pressure in the SCF

High-frequency short-duration ultrasonic pulses are suitable to modulate short FBGs, reducing the grating length, size, and time response of sensors and acousto-optic modulators (AOMs). For both types of devices, the variation of the Bragg wavelength λ_B mostly depends on the acoustically induced axial strain in the fiber core ε_z, given as [16],

$$\lambda_B \Delta = \lambda_B (1 - p_e) \varepsilon_z, \tag{1}$$

which, p_e, is the elasto-optical constant [16]. We evaluated ε_z in the SCF core induced by the Gaussian-modulated pulses. Fig. 6(a)-(c) show the pulses propagating along the fiber from t = 0.1 to 2 μs (5 steps). The variation of the pulse length B_z (total spatial width where ε_z decays to null) and strain peak are shown in Fig. 7(a) and 7(b). We note that modal dispersion effects are similar to those discussed in Section 3.1. Fig. 6(a) shows the pulse at f = 25 MHz propagating with roughly constant strain peaks while inducing trailing pulses along the fiber (B_z increases about 10 times in Fig. 7(a)). In contrast, the pulses at f = 72 MHz show increasing strain peaks and reduced trailing pulses (max. B_z ~ 8.4 mm), as shown in Fig. 6(b) and 6(c). The narrow pulse (B_f = 10 MHz) provides a smaller broadening slope and significantly higher magnitudes (up to 18 times higher than the low-frequency pulse). The pulses' parameters change similarly with time, as shown in Fig. 7(c) and 7(d). We note oscillating strain magnitudes probably caused by the modes inducing beatlengths along the SCF, reallocating the strains between the cladding and core [7] (apparently, some pulses seem to fragment and further recompose). For applications with FBGs, the simulated spatiotemporal responses might be useful to predict SCF and grating lengths and propagation times to enhance FBG modulation. The results suggest that SCFs guiding low-dispersive pulses might transmit significant amplitudes over lengths longer than L = 10 mm, at the expense of increasing trailing pulses. Alternatively, SCFs with FBGs shorter than L = 2.5 mm might provide faster, shorter, and stronger pulses, increasing grating modulation and sensing efficiencies.

We have evaluated the pressure P induced by the pulses at the SCF input and output. Fig. 8(a)-(c) show the pressure confinement (ratio of pressure in the SCF cross-section (P_{SCF}) and only in the core (P_{core})). The maximum $|P|$ in the core is shown in Fig. 8(d)-(f) (2D SCF ends show null (blue) and maximum (red) $|P|$). Fig. 8(a) indicates that the pressure is mostly distributed in the SCF cladding at f = 25 MHz, reducing output pressures by 46 % (Fig. 8(d)). In contrast, P is highly confined and amplified at f = 72 MHz (Fig. 8(e)-(f)). Fig. 9(a)-(c) show the ultrasonic propagating pulses with maximum pressures at the SCF output. These achievements suggest that SCFs might offer unprecedented features to guide high-power ultrasonic signals over long distances. We expect pulses to be delivered over a few centimeters from the SCF input. Pressure peaks, widths, and confinement might however change due to increasing multimode dispersion.

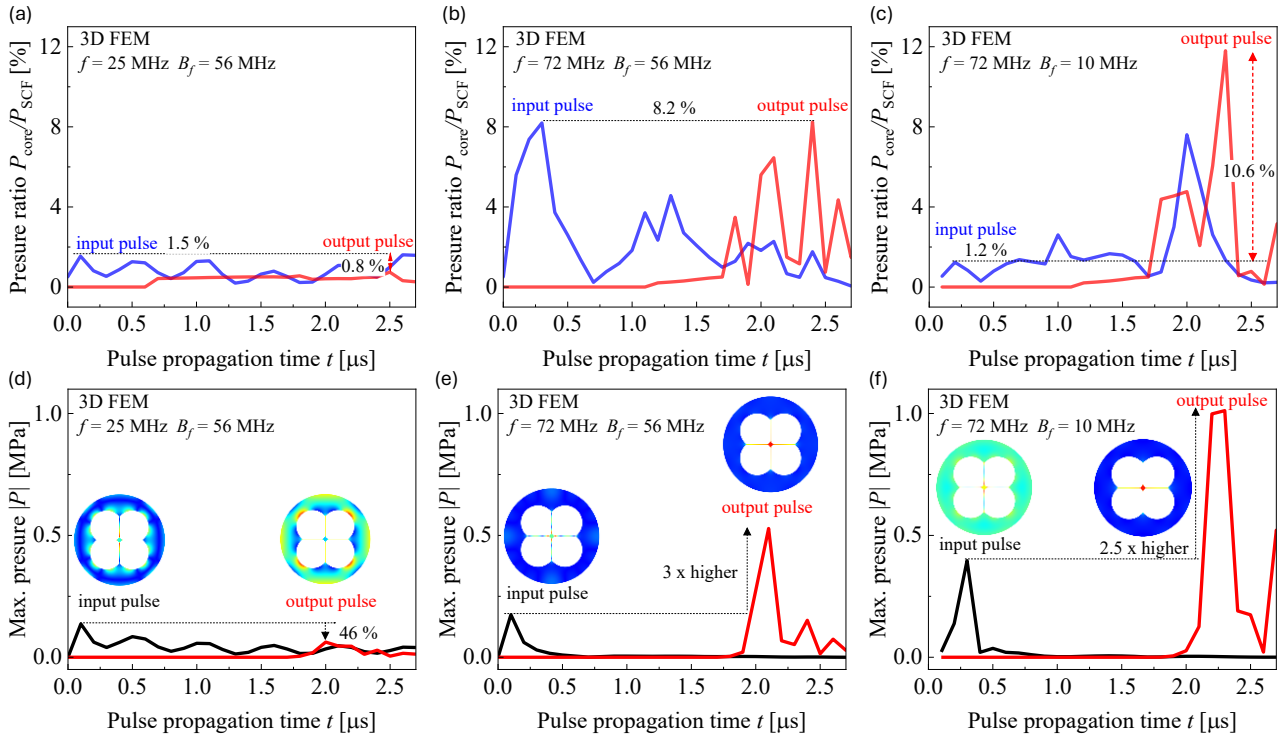

FIGURE 8. 3D FEM simulated (a)-(c) pressure confinement and (d)-(f) maximum pressure $|P|$ at the SCF input and output induced respectively by the ultrasonic pulses at f = 25 MHz (B_f = 56 MHz) and f = 72 MHz (B_f = 56 and 10 MHz) up to t = 2.7 μs (insets show the 3D SCF ends indicating null (blue) and maximum (red) pressures).

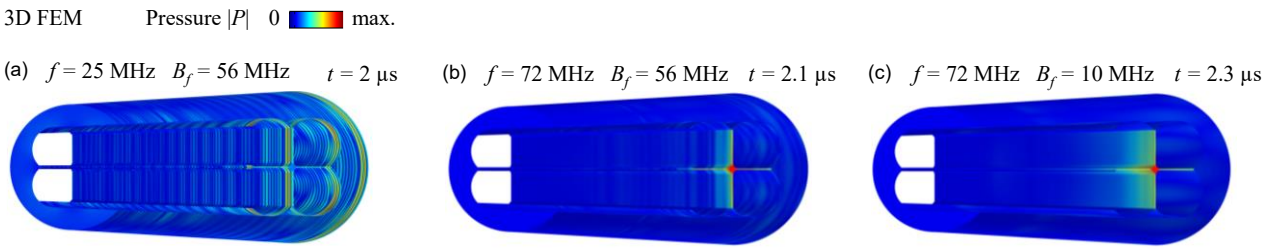

FIGURE 9. 3D FEM simulated SCF showing the maximum pressure induced by the ultrasonic pulses at fiber output: (a) f = 25 MHz (B_f = 56 MHz), (b) f = 72 MHz (B_f = 56 MHz), and (c) f = 72 MHz (B_f = 10 MHz).

4. BROADBAND ULTRASONIC SENSING OF THE SCF

We evaluate the peak strains and pressures in the SCF core from f = 1 to 100 MHz (SCF is excited over this range with a constant magnitude, monochromatic, sinusoidal input signal F at 1 MHz steps). This allows us to evaluate the ultrasound parameters in the whole spectrum compared to pulses with specific bandwidths (3D FEM modeling of this frequency response is described in Appendix A).

Fiber sensors used in optoacoustic imaging and underwater applications are usually based on phase modulation of optical modes induced by the measured ultrasound. For solid core optical fibers, the acoustically induced strains modulate the core refractive index n and fiber length L, causing a shift in the optical phase, $\varphi = 2\pi n_{eff} L/\lambda$, where, n_{eff} is the mode effective index and, λ is the optical wavelength [3], [4], [18]. The phase sensitivity, $S = d\varphi/dP$, relates to the phase change caused by the effective acoustic pressure in the fiber core P. Thus, the normalized sensor responsivity (NR) is given as [19],

$$NR = \frac{d\varphi}{\varphi dP} = \frac{1}{dP}\left[\varepsilon_z - \frac{n^2}{2}\left((p_{11}+p_{12})\varepsilon_r + p_{12}\varepsilon_z\right)\right], \quad (2)$$

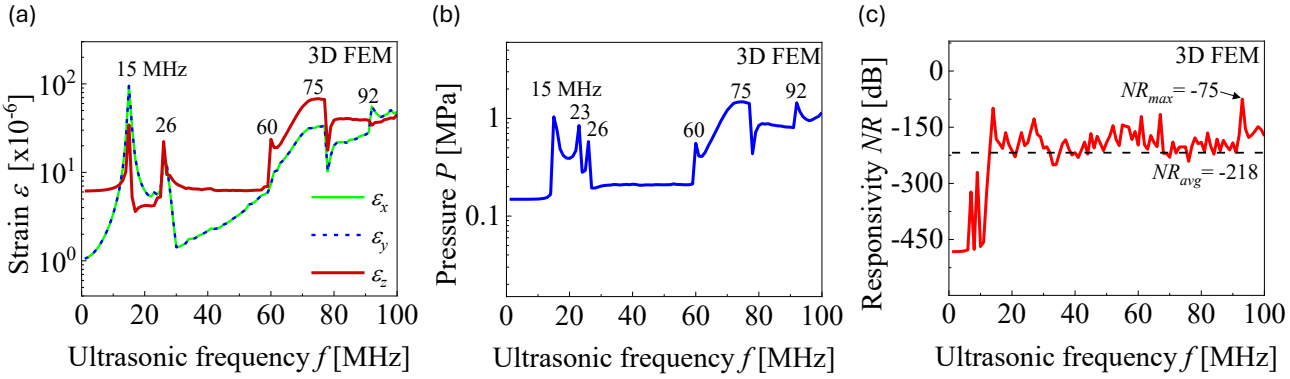

FIGURE 10. 3D FEM simulation of the (a) ultrasonically induced axial (ε_z) and radial (ε_y and ε_x) peak strains, (b) pressure P and, (c) sensing responsivity NR in the SCF core from f = 1 to 100 MHz (the highest resonances are indicated in the figures).

where, ε_z and ε_r, are respectively the axial and radial strains and, p_{11} and p_{12}, are the elasto-optic tensor coefficients [19].

Fig. 10(a) shows the simulated axial, ε_z, and radial strain peaks ($\varepsilon_r = \varepsilon_x = \varepsilon_y$) in the SCF core, indicating the highest resonances in the frequency range. Axial strains are predominant with relevant radial distribution at f = 15, 26, and 92 MHz. As discussed in Section 2, ultrasonic modes with low and similar velocities are radially distributed in the fiber. Overall, SCF provides higher strains over a broad bandwidth reducing the large gaps between resonances compared to SMFs [4], [5], [7].

Fig. 10(b) shows the peak pressure P changing similarly to the axial strain, following the contribution of axial stress components to the pressure. The responsivity, NR, is computed with (2) in dB (20Log (NR) [20]), as shown in Fig. 10(c). We note that SCF provides a flatter and higher NR bandwidth (86 MHz) compared to previous studies using HCFs [14]. The maximum and average responsivities are NR_{max} = -75 dB (at f = 93 MHz) and NR_{avg} = -218 dB. This wide and high responsivity might improve the spatial resolution of practical devices in strong attenuation ranges, favoring the measurement of microscale details in biomedical applications. The increased strains, pressures, and NR might be caused by the effective single-mode SCF core, and the reduced silica in the SCF cross-section. Higher strains and pressures with increasing input power are expected. The estimated parameters should be useful to predict the sensing performance of SCFs with distinct FBGs, Fabry-Perot, and Michelson interferometers [21], [22].

5. OUTLOOK FOR NEXT-GENERATION ALL-FIBER ULTRASONIC DEVICES

We have investigated the propagation and confinement of broadband high-frequency ultrasound in a four-air hole SCF. The time and frequency responses of the ultrasonic signals were evaluated along a 10 mm fiber length from f = 1 to 100 MHz. Next, we summarize the main achievements and contributions, highlighting their significance in advancing cutting-edged fiber-based ultrasonic devices.

The modal dispersion is characterized by the variation of modes' group velocity, wavenumber, and period with increasing frequency. The dispersion curves might be used to predict the modal spatial distribution, polarization, and interference regardless of fiber length or input signal power. 2D simulations indicate these modal properties depend only on the SCF geometry, material, and excitation frequency. For practical applications, the simulated modal parameters are important for designing low-dispersive ultrasonic SCF devices, providing high-peak powers and reduced-width propagating pulses. Besides, the modal parameters might be used to calculate the acoustic impedances required to match components or layers attached to the SCF surface [23].

The spatial-temporal propagation of Gaussian-modulated pulses typical of those used in experiments was evaluated at distinct frequencies and bandwidths, showing that the pulses' duration and spatial length considerably broaden along the fiber and with time. Broad pulses (56 MHz) centered in high dispersive ranges (25 MHz) show reduced magnitudes and broad widths compared to high-frequency (72 MHz) narrow (10 MHz) pulses. This suggests the use of short SCFs (< 2.5 mm) and fast pulses (t = 500 ns) to achieve higher strains and sensitivities in the SCF core, further benefiting strong modulation of FBGs and interferometers.

For applications in optoacoustic fiber sensors, SCFs appear to provide flatter and higher sensing responsivities (NR) over a broad ultrasound spectrum (86 MHz) compared to SMFs. Moreover, SCFs offer better mechanical stability than fiber tapes and etched fibers, increasing spatial resolution. The axial ultrasonic excitation and propagation might enable simultaneous light-sound guidance in the SCF core, guiding laser pulses to biological tissues while measuring the optically generated ultrasound. We expect that SCFs might be integrated with endoscopes, catheters, and minimally-invasive needles, reducing the number of components, equipment, and costs (practical sensors are usually transversally excited or use two fibers to guide separately acoustic and optic signals [2], [3]). The SCF's high responsivity could also find applications in metrology, spectroscopy, underwater acoustic signals, and gas detection [24].

SCF properties might also benefit optoacoustic transmitters employed in neurostimulation, by delivering high-power, focused ultrasound to stimulate neurons. Absorbers such as carbon nanotubes (CNTs) might be deposited inside the SCF, reducing biological exposition to thermochemical effects compared to devices based on SMFs (where optical absorbers at the fiber tip heat the tissue [10], [11]). CNTs confined in the SCF air holes would also improve laser absorption from the fiber core, reducing the dissipated power and absorber's material. Besides, highly amplified pulses propagating along SCF lengths might be focused on spots comparable to the core diameter (5 μm). Strong pulses at the SCF output could contribute to overcoming the excessive attenuation in tissues, permitting pulses to travel long distances to their target. Thus, these achievements might also find unprecedented applications in ultrasonic microsurgery.

Finally, SCFs might be combined with FBGs for application in all-fiber acousto-optic modulators (AOMs), which enables electrical tuning of the power, wavelength, and repetition rate of pulsed fiber lasers [15], [25]. In this case, SCFs might significantly increase the frequency and repetition rate of practical devices (currently working up to 15 MHz) while reducing fiber and grating lengths (12 cm FBGs are modulated by low-frequency ultrasonic pulses (2.5 cm pulse length) [25]). Acoustic drivers exciting single or narrowband low dispersive ultrasonic signals would improve ultrasound modulation of FBGs, enabling tunable fiber lasers with repetition rates higher than 200 MHz.

Overall, our study considers an ideal SCF and experimental ultrasonic magnitudes and bandwidths might change due to fiber geometry deviations, damping, and perturbations induced by external agents (e.g., by pressing or bending the SCF). In addition, combining SCF with drivers, absorbers, interferometers, coatings or other components might affect the predicted temporal or frequency responses. Therefore, the influence of layers or tissues attached to the SCF should be further investigated. Future research should also consider SCFs with distinct geometries, larger holes, reduced cores, and thinner bridges to enhance ultrasonic signals, contributing to compact, fast, and efficient all-fiber devices operating beyond 100 MHz.

6. CONCLUSION

We have numerically and analytically demonstrated the spatial-temporal tunneling of ultrasonic modes inside a suspended core fiber for the first time. An experimentally-based SCF is modeled along 10 mm employing the 2D and 3D finite element methods. The ultrasonic modes' velocity, wavenumber, and period are evaluated from 1 to 100 MHz, indicating 11 modes interfering in the SCF. The modal parameters are estimated in the SCF core using the recognized Pochhammer-Chree analytical formulation. FEM and analytical results suggest that the modes rearrange their distribution to provide effective single-mode propagation in the SCF core (theoretically, the 5 μm core diameter cannot support more than one mode at the considered frequencies).

Gaussian-modulated pulses propagating at different center frequencies (25 and 72 MHz) and bandwidths (56 and 10 MHz) are evaluated along the SCF length as a function of time. The input pulse at 25 MHz shows decreasing displacements, strains, and pressures with increasing propagation time and length, causing low-amplitude trailing pulses. This might be caused by modes interfering radially, concentrating energy mainly in the SCF cladding. In contrast, the pulses at 72 MHz provide significantly amplified magnitudes and narrower spatial and temporal widths. In this case, narrow pulses (10 MHz) might emphasize single-mode guidance, confining and amplifying strains (18 times) and pressures (3 times) compared to low-frequency pulses.

Overall, compared to SMF, the SCF shows flatter and higher strains and pressures over the wide spectral range of 86 MHz, with distinct sensing responsivities (-218 dB average and -75 dB maximum at 93 MHz). To the best of our knowledge, this is the widest high-responsivity bandwidth reported. These achievements reveal contributions from exceptional single-mode propagation in the suspended core and reduced silica in the SCF, suggesting larger air holes, smaller cores, and thinner bridges could further improve light-sound interaction. Thus, SCFs can potentially overcome ultrasonic attenuation in practical devices, leading to high efficiency, spatial resolution, and miniaturization of optoacoustic fiber sensors, neurotransmitters, and acousto-optic modulators.

APPENDIX A - NUMERICAL AND ANALYTICAL MODELING OF THE SCF

SCF is modeled using the FEM-based Structural Mechanics Module included in COMSOL Multiphysics 5.4. The 2D model is based on a pure silica experimental SCF [26] composed of a 5 μm diameter core suspended by four air holes of 45 μm in diameter. The bridges are 27 μm long and 700 nm in thickness. The SCF outer diameter is 125 μm.

The SCF silica regions are modeled with the properties: Young's modulus, $Y = 72.5$ GPa, Poisson's ratio, $\nu = 0.17$, density, $\rho = 2200$ kg/m^3 [16]. The displacement patterns of the ultrasonic axially symmetric modes are computed using the 2D SCF from $f = 1$ to 100 MHz (5 MHz steps). The modes' wavenumber k, group velocity c_g, and wavelength Λ are computed for the range with 20 kHz steps using a quarter of the 2D geometry as described in [7]. These simulations are performed with a desktop computer with a 3.2 GHz Intel i7 processor (6 cores) and 64 GB memory.

The 3D SCF model is designed by extruding the 2D geometry along $L = 10$ mm. A perfectly matched layer (PML) with 100 µm thickness is set at the SCF output to prevent reflection of propagating waves at the fiber end interface [7]. The remaining SCF surfaces are tension-free, and no ultrasound power dissipation is considered. A sinusoidal force with $F_0 = 3\times10^{-3}$ N is axially applied at the SCF input from $f = 1$ to 100 MHz (1 MHz step) and the ultrasonic modes are simultaneously excited. The period Λ is calculated using the amplitude peak-to-peak method (APP) and the fast Fourier transform (FFT) of the induced axial displacements at the SCF core center (fiber radius $r = 0$) [7]. APP averages the distance between the wave nodes and peaks while FFT converts the wave along the spatial domain z to the spatial frequency domain ($f_z = z^{-1}$). The induced pressure P, axial (ε_z), and radial (ε_x, ε_y) strains peaks and sensing responsivity NR are estimated in the SCF core (NR using (2) in Section 4).

The Gaussian-modulated ultrasonic pulses are modeled using the same 3D SCF model using a time-dependent study. The input pulses are described as [27],

$$F(t) = F_0 \exp\left[-\frac{1}{2}\left(\frac{t-t_0}{\sigma}\right)^2\right]\cos\left(2\pi f(t-t_0)\right) \tag{3}$$

where, f, is the central frequency, $t_0 = 3\sigma$, is the temporal pulse shift, $\sigma = 1/B_f$, is the standard deviation, and B_f is total frequency width. Three pulses are modeled: one at $f = 25$ MHz ($B_f = 56$ MHz), and two at $f = 72$ MHz ($B_f = 56$ and 10 MHz). The signal peak magnitude F_0 and other modeling constraints are the same as those used for the frequency response described above.

The axially induced displacement w is evaluated at the SCF ends (averaged over the core cross-section) from $t = 0$ to 2.7 µs (1.92 ns steps). Similarly, the induced axial strains ε_z are assessed along L from $t = 0.1$ to 2 µs (5 steps). The pressure confinement (P_{core}/P_{SCF}) is estimated by integrating the pressure modulus $|P|$ over the SCF cross-section (P_{SCF}) and in the core (P_{core}). The maximum $|P|$ is measured in the core ends (0.1 µs steps). 3D FEM simulations are performed using a high-performance computer (HPC) equipped with 2000 processor cores and 9 TB memory.

The propagation of ultrasonic modes in the SCF core is defined by the Pochhammer-Chree frequency equation, written as [28], [29],

$$k^2\frac{qJ_0(qr)}{J_1(qr)} - \frac{1}{2r}\left(\frac{\omega}{c_T}\right)^2 + \left[\frac{1}{2}\left(\frac{\omega}{c_T}\right)^2 - k^2\right]^2 \frac{J_0(pr)}{pJ_1(pr)} = 0, \tag{4}$$

in which, $p^2 = \omega^2 c_D^{-2} - k^2$, $q^2 = \omega^2 c_T^{-2} - k^2$, r is the fiber radius ($2r = 5$ µm is the inscribed circle SCF core diameter), $\omega = 2\pi f$, is the angular frequency, $c_D^2 = (\gamma + 2\mu)/\rho$, and, $c_T^2 = \mu/\rho$, are the dilatational and transversal velocities, $k = 2\pi\Lambda^{-1}$, is the wavenumber and, Λ, is the wavelength. J_0 and J_1 are the zero and first order Bessel functions of first kind, and γ and μ, are the Lame elastic constants (calculated from the silica properties described in FEM modeling) [16]. Equation (4) is valid for a solid, isotropic, homogeneous, and linearly elastic core). This modeling assumes that the acoustic properties do not significantly change over the SCF core cross-section. The modal wavenumber k is computed from the roots of (4) up to $f = 100$ MHz, employing the algorithms developed in [27], [29]. The period Λ and group velocity, $c_g = \partial k/\partial\omega$, are derived from k. The analytical simulations indicate the propagation of a unique ultrasonic mode in the SCF core in the considered frequency range. FEM and analytical velocities are compared to the silica's extensional velocity, $c_E^2 = Y/\rho$, and Rayleigh surface velocity, $c_R \sim ((0.87 + 1.12\upsilon)/(1+\upsilon))\, c_T$ [7]. The complete step-by-step guide for 2D, 3D FEM, and analytical modeling is found in [7].

ACKNOWLEDGMENT

This work was supported in part by the grant 2022/10584-9, São Paulo Research Foundation (FAPESP) and partly funded by the European Union´s Horizon 2020 research and innovation programme under the Marie Sklodowska-Curie grant agreement No 713694. We acknowledge the use of Athena at HPC Midlands+, which was funded by the EPSRC on grant EP/P020232/1 as part of the HPC Midlands+ consortium.

REFERENCES

[1] A. Taruttis and V. Ntziachristos, "Advances in real-time multispectral optoacoustic imaging and its applications," *Nature Photonics 2015 9:4*, vol. 9, no. 4, pp. 219–227, Mar. 2015, doi: 10.1038/nphoton.2015.29.

[2] C. D. Little *et al.*, "Optically generated ultrasound for intracoronary imaging," *Front Cardiovasc Med*, vol. 7, p. 525530, Oct. 2020, doi: 10.3389/FCVM.2020.525530/BIBTEX.

[3] A. Rosenthal *et al.*, "Fiber interferometer for hybrid optical and optoacoustic intravital microscopy," *Optica*, vol. 4, no. 10, pp. 1180–1187, Oct. 2017, doi: 10.1364/OPTICA.4.001180.

[4] I. A. Veres, P. Burgholzer, T. Berer, A. Rosenthal, G. Wissmeyer, and V. Ntziachristos, "Characterization of the spatio-temporal response of optical fiber sensors to incident spherical waves," *J Acoust Soc Am*, vol. 135, no. 4, p. 1853, May 2014, doi: 10.1121/1.4868391.

[5] T. Berer, I. A. Veres, H. Grün, J. Bauer-Marschallinger, K. Felbermayer, and P. Burgholzer, "Characterization of broadband fiber optic line detectors for photoacoustic tomography," *J Biophotonics*, vol. 5, no. 7, pp. 518–528, Jul. 2012, doi: 10.1002/JBIO.201100110.

[6] I. A. Veres *et al.*, "Numerical and analytical modeling of optical fibers for ultrasound detection," *IEEE International Ultrasonics Symposium, IUS*, pp. 520–523, 2011, doi: 10.1109/ULTSYM.2011.0125.

[7] R. E. Silva and D. J. Webb, "Detailed spatial-spectral numerical characterization of axially symmetric broadband ultrasonic resonances in standard optical fibers," *Optical Fiber Technology*, vol. 75, p. 103192, Jan. 2023, doi: 10.1016/J.YOFTE.2022.103192.

[8] R. E. Silva, A. Hartung, M. Rothhardt, A. A. P. Pohl, and H. Bartelt, "Detailed numerical investigation of the interaction of longitudinal acoustic waves with fiber Bragg gratings in suspended-core fibers," *Opt Commun*, vol. 344, pp. 43–50, Jun. 2015, doi: 10.1016/j.optcom.2015.01.037.

[9] R. E. Silva and D. J. Webb, "Ultra-efficient in-core acoustic waves in suspended core fiber for high frequency fiber-optic ultrasonic devices," *Applied Physics Express*, vol. 14, no. 8, p. 087003, Aug. 2021, doi: 10.35848/1882-0786/AC17D5.

[10] Y. Jiang *et al.*, "Optoacoustic brain stimulation at submillimeter spatial precision," *Nat Commun*, vol. 11, no. 1, pp. 1–9, Feb. 2020, doi: 10.1038/s41467-020-14706-1.

[11] L. Shi *et al.*, "Non-genetic photoacoustic stimulation of single neurons by a tapered fiber optoacoustic emitter," *Light Sci Appl*, vol. 10, no. 1, pp. 1–13, Jul. 2021, doi: 10.1038/s41377-021-00580-z.

[12] L. Shi, Y. Jiang, N. Zheng, J.-X. Cheng, and C. Yang, "High-precision neural stimulation through optoacoustic emitters," *Neurophotonics*, vol. 9, no. 3, p. 032207, Mar. 2022, doi: 10.1117/1.NPH.9.3.032207.

[13] R. E. Silva *et al.*, "Numerical investigation of the interaction of tubular hollow-core fibers and flexural acoustic waves," *Journal of Lightwave Technology*, Mar. 2025, doi: https://doi.org/10.1109/JLT.2025.3549948.

[14] R. E. Silva, D. J. Webb, C. M. B. Cordeiro, and M. A. R. Franco, "Highly amplified broadband ultrasound in antiresonant hollow core fibers," *Adv Photonics Res*, vol. 6, no. 2, p. 2400086, Feb. 2025, doi: 10.1002/ADPR.202400086.

[15] R. E. Silva *et al.*, "Acousto-optic modulation of a fiber Bragg grating in suspended core fiber for mode-locked all-fiber lasers," *Laser Phys Lett*, vol. 12, no. 4, p. 045101, Apr. 2015, doi: 10.1088/1612-2011/12/4/045101.

[16] P. T. Neves Jr. and A. A. P. Pohl, "Time analysis of the wavelength shift in fiber Bragg gratings," *Journal of Lightwave Technology*, vol. 25, no. 11, pp. 3580–3588, 2007, doi: 10.1109/JLT.2007.907744.

[17] A. D. Puckett and M. L. Peterson, "Individual longitudinal Pochhammer-Chree modes in observed experimental signals," *Acoustic Research Letters Online*, vol. 6, no. 4, pp. 268–273, Oct. 2005, doi: 10.1121/1.2033088.

[18] J. Dorighi, S. Krishnaswamy, and J. D. Achenbach, "Response of an embedded fiber optic ultrasound sensor," *J Acoust Soc Am*, vol. 101, no. 1, p. 257, Jun. 1998, doi: 10.1121/1.417997.

[19] A. Abdallah, C. Zhang, and Z. Zhong, "Phase sensitivity to acoustic pressure of microstrustured optical fibers: a comparison study," *International Journal of Signal Processing, Image Processing and Pattern Recognition*, vol. 8, no. 2, pp. 105–114, Feb. 2015, doi: 10.14257/IJSIP.2015.8.2.11.

[20] A. Abdallah, C. Z. Zhang, and Z. Zhong, "Acoustic Pressure Sensing with Hollow-Core Photonic Bandgap Fibers," *Applied Mechanics and Materials*, vol. 738–739, pp. 61–64, Mar. 2015, doi: 10.4028/WWW.SCIENTIFIC.NET/AMM.738-739.61.

[21] G. Wissmeyer, M. A. Pleitez, A. Rosenthal, and V. Ntziachristos, "Looking at sound: optoacoustics with all-optical ultrasound detection," *Light Sci Appl*, vol. 7, no. 1, pp. 1–16, Aug. 2018, doi: 10.1038/s41377-018-0036-7.

[22] M. Pang and W. Jin, "Detection of acoustic pressure with hollow-core photonic bandgap fiber," *Opt Express*, vol. 17, no. 13, pp. 11088–11097, Jun. 2009, doi: 10.1364/OE.17.011088.

[23] Jan. Achenbach, *Wave Propagation in Elastic Solids.*, 1st ed. Elsevier Science, 1984.

[24] Q. Wang *et al.*, "Dual-comb photothermal spectroscopy," *Nat Commun*, vol. 13, no. 1, pp. 1–7, Apr. 2022, doi: 10.1038/s41467-022-29865-6.

[25] M. Delgado-Pinar, A. Díez, J. L. Cruz, and M. V. Andrés, "Single-frequency active Q-switched distributed fiber laser using acoustic waves," *Appl Phys Lett*, vol. 90, no. 17, p. 171110, Apr. 2007, doi: https://doi.org/10.1063/1.2732832.

[26] R. E. Silva, M. Becker, A. Hartung, M. Rothhardt, A. A. A. P. P. Pohl, and H. Bartelt, "Reflectivity and bandwidth modulation of fiber Bragg gratings in a suspended core fiber by tunable acoustic waves," *IEEE Photonics J*, vol. 6, no. 6, pp. 1–8, Dec. 2014, doi: 10.1109/JPHOT.2014.2366161.

[27] A. Puckett, "An experimental and theoretical investigation for axially symmetric wave propagation in thick cylindrical waveguides," 2004. Accessed: Dec. 28, 2020. [Online]. Available: http://digitalcommons.library.umaine.edu/etd/285

[28] M. Redwood, "Velocity and attenuation of a narrow-band, high-frequency compressional pulse in a solid wave guide," *J Acoust Soc Am*, vol. 31, no. 4, p. 442, Jul. 2005, doi: 10.1121/1.1907732.

[29] M. L. Peterson, "Prediction of longitudinal disturbances in a multimode cylindrical waveguide," *Exp Mech*, vol. 39, no. 1, pp. 36–42, 1999, doi: 10.1007/BF02329299.